

Noise reduction in ISAR imaging of UAVs using weighted atomic norm minimization and 2D-ADMM algorithm

Mohammad Roueinfar^{*}, Mohammad Hossein Kahaei¹,

¹ School of Electrical Engineering, Iran University of Science and Technology, Tehran, Iran

^{*} mrooein@hotmail.com

Abstract

The effect of noise on the Inverse Synthetic Aperture Radar (ISAR) with sparse apertures is a challenging issue for image reconstruction with high resolution at low Signal-to-Noise Ratios (SNRs). It is well-known that the image resolution is affected by the bandwidth of the transmitted signal and the Coherent Processing Interval (CPI) in two dimensions, range and azimuth, respectively. To reduce the noise effect and thus increase the two-dimensional resolution of Unmanned Aerial Vehicles (UAVs) images, we propose the Fast Reweighted Atomic Norm Denoising (FRAND) algorithm by incorporating the weighted atomic norm minimization. To solve the problem, the Two-Dimensional Alternating Direction Method of Multipliers (2D-ADMM) algorithm is developed to speed up the implementation procedure. Assuming sparse apertures for ISAR images of UAVs, we compare the proposed method with the Multiple Signal Classification (MUSIC), Cadzow, and SL_0 methods in different SNRs. Simulation results show the superiority of FRAND at low SNRs based on the Mean-Square Error (MSE), Peak Signal-to-Noise ratio (PSNR) and Structural Similarity Index Measure (SSIM) criteria.

1 Introduction

The use of Unmanned Aerial Vehicle (UAV) has expanded significantly in various applications, such as monitoring forest fires, firefighting, aerial photography, product delivery, transportation, agriculture, traffic control, infrastructure inspection, etc. [1], [2], [3], [4]. Along with progressive research on this area, there are also some concerns about the unauthorized use of UAVs, which pose threats such as invasion of privacy of people and places, and destruction [5], which motivates more investigation on this area more seriously. To do so, different methods using sound, heat, optics, and radar have been presented. However, due to the low flight altitude, low heat, and weak sound of UAVs, the detection procedure becomes more difficult especially when the distance between the UAV and the detector is long [6]. In [7], long-wave infrared thermal radiation is used for UAV detection at night. In general, optical methods are more suitable for the detection and classification of small UAVs at short ranges, but they suffer from low or variable lights and also obstacles effects. Also, sound detection methods used for the direction of arrival-based identification are effectively appropriate for short distances, and distinguishing small UAVs like quadcopters from birds [8]. Radio or passive methods that use the downlink signal of quadcopters for detection may increase false alarms due to interference [9].

The Laser Imaging Detection and Ranging (LIDAR) technique, which operates by emitting laser pulses, is very sensitive to weather conditions, smoke, and direct sunlight [8]. In contrast, radar-based methods are more effective for detecting quadcopters [8], as they are immune to light and adverse weather conditions. For example, in [10], an Frequency Modulation Continuous Wave (FMCW) method is used to detect the micro-Doppler pattern caused by the UAV rotor. In [11], the impact of frequency, polarization, and other parameters on ISAR images is investigated using the radar signature of small drones. Also, an FMCW radar network has been developed by [8] to detect and classify multi-rotor UAVs.

In some applications, high-resolution imaging of UAVs is required under various weather conditions. An effective method applied for aerial targets is the Inverse Synthetic Aperture Radar (ISAR) [12], which produces two-dimensional images of moving targets in the range and azimuth directions. These images are created by the echo signals of target scatterers received from different angles and also processing the Doppler frequency caused by the target motion. Using the squint minimization technique in FMCW ISAR, the large trajectory deviations of UAVs are reduced, [13]. In [14] for accurate detection and positioning of UAV swarms, a method based on the Dechirp-keystone transform and frequency-selective reweighted trace minimization is developed. A tracking-before-detection algorithm is reported in [15] for UAV tracking based on multiple ellipses or a sub-random matrices model with non-linear ISAR observations and unknown orientation angle due to the Doppler effect. In [16], a method is presented for UAV imaging based on an improved complex variable mode decomposition approach and using a microwave photonic ISAR.

As known, the amplitude of scattered signals is related to the target Radar Cross Section (RCS) [17], and the resolution in range and azimuth directions depends on the transmit signal bandwidth and the CPI, respectively. Effectively, the wider the bandwidth, the more resolution in the range direction is achieved. In practice, however, the bandwidth and CPI are limited and can not be increased to the desired amounts. From another aspect, it is well known that for retrieving ISAR images, scatterer points with higher RCS are the most effective and generally sparse. Moreover, some radar pulses may be missed during transmission/reception, or due to maneuvers of the target leading to sparse apertures, which can result in blurred images [18]. To improve the ISAR image resolution in such situations, we can exploit the target sparsity and sparse apertures in the spatial domain.

This leads to super-resolution methods, which are divided into on-grid, off-grid, and gridless methods. In the first case, we consider a set of discrete fixed points and assume the target scatterers are located on them. Then, the resolution is improved for a larger number of grids, which in turn increases the complexity. In the off-grid method, the distances between the pre-determined grids and scatterers are estimated simultaneously and included in computations, which normally results in a complicated implementation. The gridless method, also known as the continuous compressed sensing method, is defined using Atomic Norm Minimization (ANM), where, unlike the previous two methods, a set of continuous atoms is defined based on the received signal (echo). It is assumed that the echoes of target scatterers are linearly combined, where each echo is represented by an atom that is a complex exponential vector whose amplitude and phase are proportional to the RCS and phase of each echo, respectively. By applying convex minimization to the problem, the atoms, target scatterers, and finally the target image are obtained. The gridless method with ANM has been applied for ISAR imaging in [19], [20], and [21]. Also, [22], [23], and [24] have presented some methods to reduce the noise effect at low SNRs.

In this paper, we propose the FRAND method by incorporating the weighted atomic norm to reduce the noise effect and increase the resolution in ISAR imaging. The paper

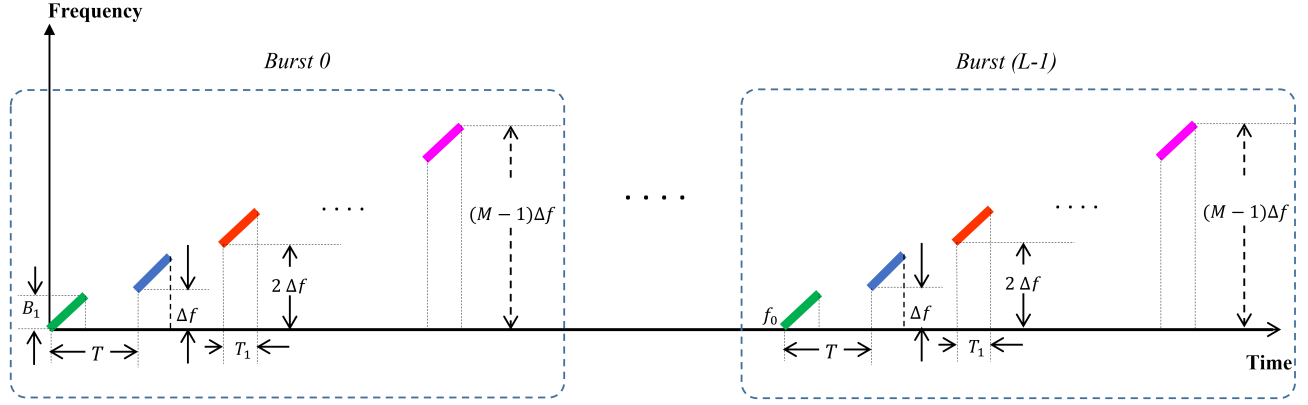


Fig 1. FSCS time-frequency diagram.

is organized as follows. In Section 2, the signal model is defined. The FRAND method is introduced in Section 3 and the corresponding simulation results are presented in Section 4. Section 5 concludes the paper.

2 Signal Model

The relative motion between a radar and target results in translational and rotational motions, which lead to blurring and range-variant phase errors in ISAR imaging, respectively [25]. In this work, we assume both translational and rotational motions are compensated. Also, we use the Frequency Stepped Chirp Signal (FSCS) shown in Fig 1. This signal is active in L specific and equal time intervals (L bursts), where each burst consists of M pulses with Linear Frequency Modulation (LFM), B_1 shows the frequency bandwidth of each pulse, Δf is the size of the frequency step, T_1 is the pulse duration, M is the number of frequency steps, and $\frac{1}{T}$ determines the Pulse Repetition Frequency (PRF). It is well-known in pulse compression radars that the range resolution is inversely proportional to the transmitted signal bandwidth. In the FSCS structure, the bandwidth of an LFM is split into some narrowband sub-chirps, and after properly processing this waveform with the echoes, the bandwidth of the composite signal at the matched filter output effectively is increased, which consequently improves the range resolution. Also, due to the use of narrowband sub-chirps in this waveform, other radar transmitters have the least interference.

Mathematically, the m -th pulse of the l -th burst for $l = 0, 1, \dots, L - 1$ and $m = 0, 1, \dots, M - 1$ is defined as

$$s_T(t, m; l) = x(t - (lM + m)T) \exp[j2\pi f_m(t - (lM + m)T)], \quad (1)$$

where $x(t) = \text{rect}(\frac{t}{T_1}) \exp[j\pi\gamma t^2]$, T_1 is the pulse width, $\gamma = \frac{\Delta f}{T_1}$ is the chirp rate, $f_m = f_0 + m\Delta f$ is the carrier frequency of the m -th pulse with f_0 showing the initial frequency, and Δf is the frequency step. Accordingly, the received signal composed of K scatterers is described as

$$r_T(t, m; l) = \sum_{k=0}^{K-1} \sigma_k x(t - \tau_k(t) - (lM + m)T) \exp[j2\pi f_m(t - \tau_k(t) - (lM + m)T)], \quad (2)$$

where σ_k is the reflection coefficient, $\tau_k(t) = \frac{2R_k(t_n)}{c}$ is the delay it takes the ISAR signal to travel to the k -th scatterer and return, with $R_k(t_n)$ being the instantaneous distance

at the discrete observation time, t_n , $n = 0, 1, \dots, N - 1$, in the azimuth direction for the signal received from angle θ_n . Then, after dechirping, the received signal is obtained as

$$r(f_m, t_n) = \sum_{k=0}^{K-1} \sigma_k \exp \left[-j2\pi f_m \left(\frac{2R_k(t_n)}{c} \right) \right]. \quad (3)$$

By associating the rotational motion of the target at the coordinates (x_k, y_k) , the instantaneous range of ISAR to the center of the k -th scatterer is measured as

$$R_k(t_n) = \sqrt{R_0^2 + x_k^2 + y_k^2 + 2R_0[x_k \sin(\omega t_n) + y_k \cos(\omega t_n)]}, \quad (4)$$

where ω is the angular velocity and R_0 shows the distance between the center of the target and radar. Since this distance is usually large; that is the target is in far field, we can approximate Eq(4) as

$$R_k(t_n) \approx R_0 + x_k \sin(\omega t_n) + y_k \cos(\omega t_n), \quad (5)$$

which can be accordingly presented as

$$R_k(t_n) \approx R_0 + x_k \sin(\theta_n) + y_k \cos(\theta_n), \quad (6)$$

with $\theta_n = \omega t_n$ showing the observation angle at t_n .

By substituting Eq(6) in Eq(3), the received signal model can be written as

$$r(f_m, \theta_n) = \exp \left[-j4\pi f_m \frac{R_0}{c} \right] \sum_{k=0}^{K-1} \sigma_k \exp \left[-j4\pi f_m \frac{x_k \theta_n}{c} \right] \exp \left[-j4\pi f_m \frac{y_k}{c} \right], \quad (7)$$

where we assumed the rotation angle θ_n is typically small to use the approximations $\sin(\theta_n) \approx \theta_n$ and $\cos(\theta_n) \approx 1$. Furthermore, to compensate for the translational motion, we multiply Eq(7) by $\exp \left[j4\pi f_m \frac{R_0}{c} \right]$ to model the received signal at the n -th observation angle and m -th pulse as

$$r(f_m, \theta_n) = \sum_{k=0}^{K-1} \sigma_k \exp \left[-j4\pi f_m \frac{x_k \theta_n}{c} \right] \exp \left[-j4\pi f_m \frac{y_k}{c} \right]. \quad (8)$$

3 Proposed FRAND method

We present a method to reduce the noise effect and enhance the resolution of ISAR images. To do so, we first define the following parameters:

$$h_n = \frac{4\pi f_m}{c} \theta_n \approx \frac{4\pi f_0}{c} \theta_n \quad \text{and} \quad h_m = \frac{4\pi f_m}{c} \quad (9)$$

where $f_m = f_0 + m\Delta f$ and the imposed approximation is acceptable since θ_n 's are small. By substituting Eq(9) in Eq(8), the received signal reduces to

$$r(\theta_n, f_m) = \sum_{k=0}^{K-1} \sigma_k \exp[-jh_n x_k - jh_m y_k]. \quad (10)$$

To present Eq(10) in matrix form, we introduce $\mathbf{R} \in \mathbb{C}^{N \times M}$ with the entries $[\mathbf{R}]_{n,m} = r(\theta_n, f_m)$ and the matrix of atoms for the k -th scatterer $\mathbf{A}(k) \in \mathbb{C}^{N \times M}$ with the entries

$$[\mathbf{A}(k)]_{n,m} = \exp[-jh_n x_k - jh_m y_k]. \quad (11)$$

Also, we define the atomic set as

$$\mathcal{A} = \left\{ \mathbf{A}(k) \in \mathbb{C}^{N \times M} \mid |[\mathbf{A}(k)]_{n,m}| = 1 \right\}. \quad (12)$$

Then, by vectorizing \mathbf{R} and $\mathbf{A}(k)$ as $\mathbf{r} = \text{vec}(\mathbf{R}) \in \mathbb{C}^{NM \times 1}$ and $\mathbf{a}(k) = \text{vec}(\mathbf{A}(k)) \in \mathbb{C}^{NM \times 1}$, respectively, we get

$$\mathbf{r} = \sum_{k=0}^{K-1} \sigma_k \mathbf{a}(k), \quad (13)$$

In this way, according to [20], we can express the atomic norm problem conditioned on Eq(13) as

$$\begin{aligned} \|\mathbf{r}\|_{\mathcal{A}} &= \inf \{ t > 0 : \mathbf{r} \in t \text{conv}(\mathcal{A}) \} \\ &= \inf_{\sigma_k} \left\{ \sum_{k=0}^{K-1} \sigma_k \mid \mathbf{r} = \sum_{k=0}^{K-1} \sigma_k \mathbf{a}(k), \quad \sigma_k > 0 \right\}. \end{aligned} \quad (14)$$

where $\text{conv}(\mathcal{A})$ is the convex hull of \mathcal{A} . However, to estimate \mathbf{r} , note that in practice we may not receive some observations, i.e., some pulses from some angles. As a result, we consider \mathbf{r} as the vector of complete observations and \mathbf{r}_{Ω} as the vector of incomplete observations caused by the sparse apertures in ISAR imaging, where $\Omega \subset \{0, 1, \dots, (NM - 1)\} \times 1$ is the subset of indices of all possible observations. As a result, we obtain the estimates under the latter set as

$$\hat{\mathbf{r}} = \arg \min_{\mathbf{r}} \|\mathbf{r}\|_{\mathcal{A}} \quad s.t. \quad \hat{\mathbf{r}}_{\Omega} = \mathbf{r}_{\Omega}, \quad (15)$$

which is inherently related to the observation angles and pulse frequencies in the signal model defined by Eq(9) to Eq(13). By solving this problem, the lost observation angles or frequencies of unobserved pulses are effectively recovered, which can lead to increasing ISAR image resolution at low SNRs. To simplify the solution of Eq(15), we apply theorem 1 in [20] as

$$\begin{aligned} \|\mathbf{r}\|_{\mathcal{A}} &= \arg \min_{(\mathbf{u}, t)} \left\{ \frac{1}{2} \text{Tr}(\mathcal{T}(\mathbf{u})) + \frac{1}{2} t \right\} \\ s.t. \quad & \begin{bmatrix} \mathcal{T}(\mathbf{u}) & \mathbf{r} \\ \mathbf{r}^* & t \end{bmatrix} \succeq 0, \quad \hat{\mathbf{r}}_{\Omega} = \mathbf{r}_{\Omega}, \end{aligned} \quad (16)$$

where $\mathcal{T}(\mathbf{u})$ is a hermitian Toeplitz matrix whose first column is the vector $\mathbf{u} \in \mathbb{C}^N$, $t = \sum_{k=0}^{K-1} \sigma_k$, and $\text{Tr}(\cdot)$ is the trace of a matrix.

To consider a practical scenario, we include Additive White Gaussian Noise (AWGN), \mathbf{n}_{Ω} , as follows:

$$\mathbf{z}_{\Omega} = \mathbf{r}_{\Omega} + \mathbf{n}_{\Omega}. \quad (17)$$

Based on [26] and [27], to reduce the noise effect, the following problem is defined:

$$\hat{\mathbf{r}} = \arg \min_{\mathbf{r}} \frac{1}{2} \|\mathbf{r}_{\Omega} - \mathbf{z}_{\Omega}\|_{\mathbb{F}}^2 + \lambda \|\mathbf{r}\|_{\mathcal{A}}, \quad (18)$$

where λ is the regularization parameter. Next, we modify Eq(18) by adding a weighting matrix as

$$\hat{\mathbf{r}} = \arg \min_{\mathbf{r}} \|\mathbf{r}_{\Omega} - \mathbf{z}_{\Omega}\|_{\mathbb{F}}^2 + 2\lambda \|\mathbf{W}\mathbf{r}_{\Omega}\|_{\mathcal{A}} \quad (19)$$

where

$$\mathbf{W} = (\tan(\mathcal{T}(\mathbf{u}) + \epsilon \mathbf{I})^{-1} \quad (20)$$

with ϵ showing an adjustment parameter.

According to Eq(19) and Eq(20), we can rewrite Eq(16) as

$$\begin{aligned} & \arg \min_{\mathbf{r}} \|\mathbf{r}_\Omega - \mathbf{z}_\Omega\|_{\mathbb{F}}^2 + 2\lambda \|\mathbf{W}\mathbf{r}_\Omega\|_{\mathcal{A}} = \\ & \arg \min_{(\mathbf{u}, t, \mathbf{r})} \|\mathbf{r}_\Omega - \mathbf{z}_\Omega\|_{\mathbb{F}}^2 + 2\lambda \left\{ \frac{1}{2} \text{Tr}(\mathbf{W}\mathcal{T}(\mathbf{u})) + \frac{1}{2}t \right\} \\ & \text{s.t.} \quad \begin{bmatrix} \mathcal{T}(\mathbf{u}) & \mathbf{r} \\ \mathbf{r}^* & t \end{bmatrix} \succeq 0, \quad \hat{\mathbf{r}}_\Omega = \mathbf{r}_\Omega. \end{aligned} \quad (21)$$

However, we should note that Eq(21) is computationally complex with a high execution time. To cope with the latter deficiency, here we apply the 2D-ADMM algorithm. Using [26] and the augmented Lagrangian, Eq(21) is written as

$$\begin{aligned} \mathcal{L}_\rho(t, \mathbf{u}, \mathbf{r}, \mathbf{Z}, \mathbf{\Lambda}) = & \|\mathbf{r}_\Omega - \mathbf{z}_\Omega\|_{\mathbb{F}}^2 + \lambda \left\{ \text{Tr}(\mathbf{W}\mathcal{T}(\mathbf{u})) + t \right\} \\ & + \langle \mathbf{\Lambda}, \mathbf{Z} - \begin{bmatrix} \mathcal{T}(\mathbf{u}) & \mathbf{r} \\ \mathbf{r}^* & t \end{bmatrix} \rangle + \frac{\rho}{2} \left\| \mathbf{Z} - \begin{bmatrix} \mathcal{T}(\mathbf{u}) & \mathbf{r} \\ \mathbf{r}^* & t \end{bmatrix} \right\|^2, \end{aligned} \quad (22)$$

where ρ is a penalty parameter and $\mathbf{\Lambda}$ and \mathbf{Z} are Hermitian matrices defined as [26]

$$\mathbf{\Lambda} = \begin{bmatrix} \mathbf{\Lambda}_{NM \times NM} & \mathbf{\Lambda}_{NM \times 1} \\ \mathbf{\Lambda}_{1 \times NM} & \mathbf{\Lambda}_{1 \times 1} \end{bmatrix}, \quad \text{and} \quad \mathbf{Z} = \begin{bmatrix} \mathbf{Z}_{NM \times NM} & \mathbf{Z}_{NM \times 1} \\ \mathbf{Z}_{1 \times NM} & \mathbf{Z}_{1 \times 1} \end{bmatrix}. \quad (23)$$

To start the recursive algorithm, we first initialize $\mathbf{\Lambda}^0 = \mathbf{0}$ and $\mathbf{Z}^0 = \mathbf{0}$ and use the update steps as follows:

$$\{t^{i+1}, \mathbf{u}^{i+1}, \mathbf{r}^{i+1}\} = \arg \min_{t, \mathbf{u}, \mathbf{r}} \mathcal{L}_\rho(t, \mathbf{u}, \mathbf{r}, \mathbf{Z}^i, \mathbf{\Lambda}^i), \quad (24)$$

$$\mathbf{Z}^{i+1} = \arg \min_{\mathbf{Z} \succeq 0} \mathcal{L}_\rho(t^{i+1}, \mathbf{u}^{i+1}, \mathbf{r}^{i+1}, \mathbf{Z}, \mathbf{\Lambda}^i), \quad (25)$$

$$\mathbf{\Lambda}^{i+1} = \mathbf{\Lambda}^i + \rho \left(\mathbf{Z}^{i+1} - \begin{bmatrix} \mathbf{T}'(\mathbf{u}^{i+1}) & \mathbf{r}^{i+1} \\ \mathbf{r}^{(i+1)H} & t^{i+1} \end{bmatrix} \right), \quad (26)$$

where i is the iteration number and

$$t^{i+1} = \frac{1}{2} \mathbf{Z}_{1 \times 1}^i + \frac{1}{2} (\mathbf{Z}_{1 \times 1}^i)^* + \frac{1}{\rho} (\mathbf{\Lambda}_{1 \times 1}^i - \frac{\lambda}{2}), \quad (27)$$

$$\mathbf{r}^{i+1} = \frac{1}{2\rho + 1} \left(\mathbf{Z}_0^i + 2\rho \mathbf{Z}_1^i + 2\mathbf{\Lambda}_1^i \right), \quad (28)$$

$$\mathbf{u}^{i+1} = \mathcal{T}^* \left(\mathbf{Z}_0^i + \frac{1}{\rho} \mathbf{\Lambda}_0^i - \frac{\lambda}{2\rho} \right). \quad (29)$$

According to [26], \mathbf{Z} can be updated as

$$\mathbf{Z}^{i+1} = \arg \min_{\mathbf{Z} \geq 0} + \frac{\rho}{2} \left\| \mathbf{Z} - \begin{bmatrix} \mathcal{T}^*(\mathbf{u}^{i+1}) & \mathbf{r}^{i+1} \\ \mathbf{r}^{*i+1} & \mathbf{t}^{i+1} \end{bmatrix} \right\|. \quad (30)$$

Finally, we decompose \mathbf{Z}^{i+1} into eigenvalues as

$$\mathbf{Z}^{i+1} = \mathbf{V}\mathbf{D}\mathbf{V}^*, \quad (31)$$

where \mathbf{V} is a square matrix whose j -th column corresponds to the eigenvector of the j -th eigenvalue of \mathbf{Z}^{i+1} and \mathbf{D} is a matrix whose diagonal elements are the eigenvalues of \mathbf{Z} . Then, according to [28], non-zero eigenvalues gives the frequencies of the atoms corresponding to the range and azimuth direction of target scatterers. The summary of FRAND is given in Algorithm 1.

Algorithm 1 ISAR imaging procedure for the proposed FRAND.

Input: Received signal \mathbf{r}

Output: Recovered ISAR image of the target

1. Definition of atoms $\mathbf{a}(k)$ for K scatterers.
 2. Rewriting the received signal in vector form according to Eq(13)
 3. Definition of weighted atomic norm $\|\mathbf{r}\|_{\mathcal{A}}$ according to Eq(19)
 4. Definition of weighting matrix according to Eq(20)
 5. Implementation of the proposed FRAND method according to Eq(21)
 6. Starting the 2D-ADMM method with initial values $\mathbf{\Lambda}^0 = \mathbf{0}$ and $\mathbf{Z}^0 = \mathbf{0}$
 7. Repeating Eq(25)
 8. Updating Eq(26)
 9. Updating Eq(27)
 10. Updating Eq(28)
 11. Decomposing $\mathbf{Z}^{i+1} = \mathbf{V}\mathbf{D}\mathbf{V}^*$ into eigenvalues
 12. Recovering the frequencies corresponding to the target scatterers
 13. Recovering the target image
-

4 Simulation results

We simulate the proposed FRAND method for radar imaging of a moving quadcopter. The transmit signal is an FSCS with a center frequency of 10 GHz, chirp bandwidth of 500 MHz for one burst, PRF of 6 kHz, and pulse width of 0.4μ sec. The signal is corrupted by AWGN. It is assumed that the speed of the rotor and propeller of the quadcopter is so high that their images are almost fixed. Also, the quadcopter has no rotational motion and the translational motion is assumed to be approximately linear that is compensated. The simulations are performed on an Intel (R) Core (TM) i7-10700 CPU @ 2.90 GHz processor with 16 GB of RAM.

The performance of FRAND is compared to that of the MUSIC [23], Cadzow [24], and SL_0 [27] methods. The recovered images are shown in Fig 2 for 100 to 1600 available samples at 10 dB SNR. As can be seen, even using 600 samples out of 1600 possible samples, the quadcopter can be recognized. This is due to the sparse apertures in ISAR imaging, which is obtained completely randomly. Obviously, a larger number of samples can increase the image resolution with more details.

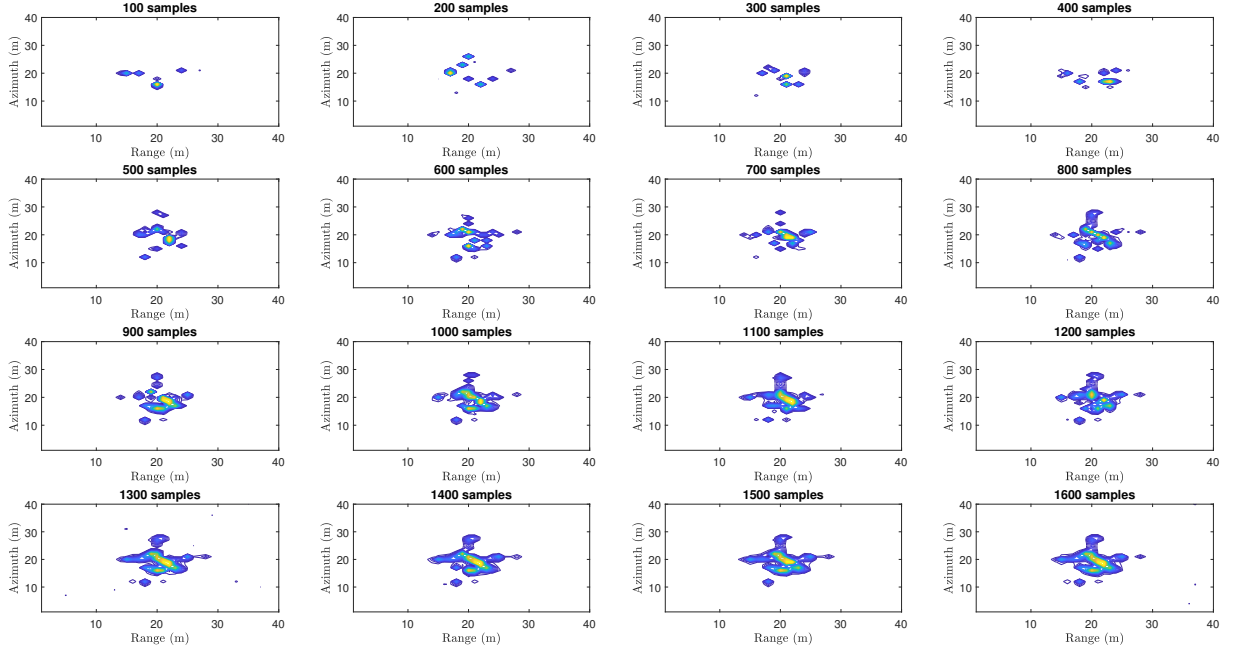


Fig 2. Recovered images of a quadcopter by FRAND using 100 to 1600 available samples at 10 dB SNR.

In Fig 3, FRAND is compared with the mentioned methods at different SNRs using 500 samples. It is seen that FRAND and SL_0 outperform the others by acceptably recovering the target image at lower SNRs; like 0 dB, due to a better noise reduction. However, when the number of samples reduces to 100, as shown in Fig 4, the performance of SL_0 gradually reduces at low SNRs, while FRAND still generates recognizable images. Next, we assess the algorithms in terms of the MSE criterion for -10 to 10 dB SNRs. The results are shown in Fig 5 by averaging 100 independent trials of the experiment for each algorithm. As can be seen, FRAND generates lower MSE than the other methods, especially at lower SNRs. The numerical values of MSEs are also given in Table 1 for a detailed comparison. These algorithms are also compared based on the Peak Signal-to-Noise ratio (PSNR) in Fig 6 by averaging 100 independent runs of each experiment. One can see that the image quality recovered by FRAND is

Table 1. MSE of SL_0 , MUSIC, Cadzow, and FRAND at different SNRs (dB).

SNR (dB)	SL_0	MUSIC	Cadzow	FRAND
-20	3.4387	2.6586	2.7280	2.2965
-15	1.3786	1.1098	1.1157	0.9427
-10	0.5596	0.4682	0.4626	0.4158
-5	0.3316	0.2588	0.2351	0.2481
0	0.3583	0.2153	0.1738	0.2131
5	0.3626	0.2205	0.1637	0.2080
10	0.3635	0.2098	0.1697	0.2072
15	0.3634	0.1982	0.1773	0.2073
20	0.3632	0.1925	0.1623	0.2071

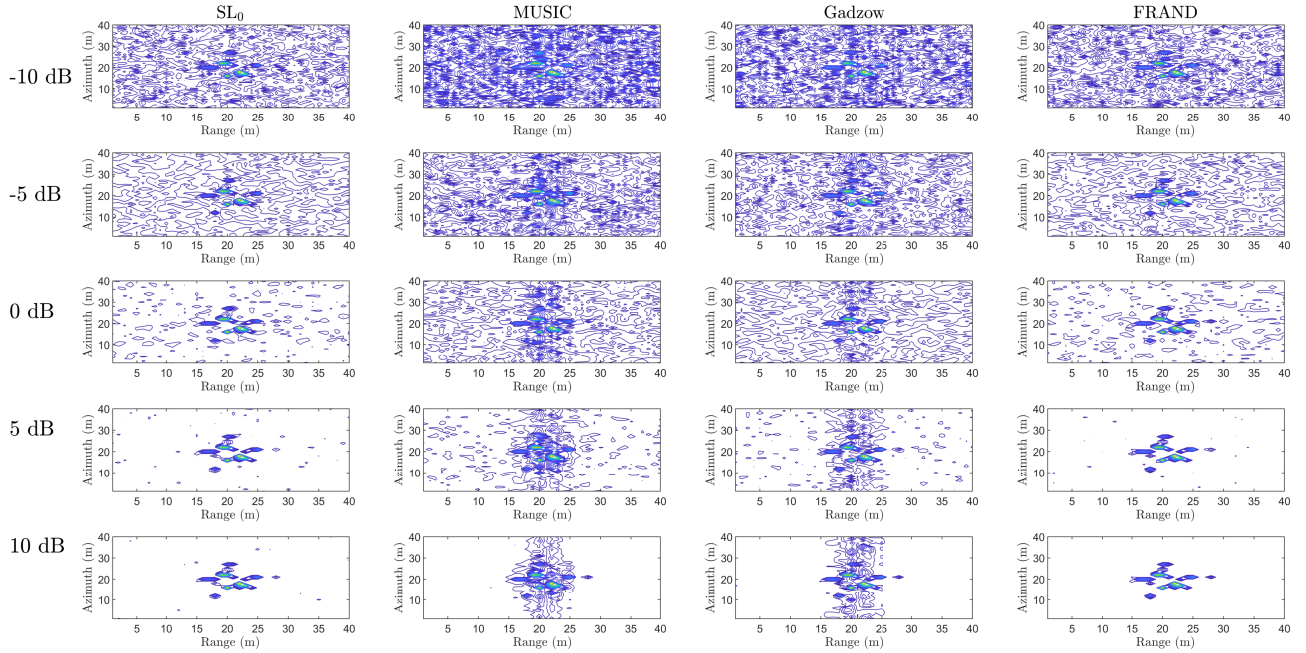


Fig 3. Recovered images of a quadcopter by SL_0 , MUSIC, Cadzow, and FRAND for 500 available samples at SNRs= -10, -5, 0, 5, and 10 dB.

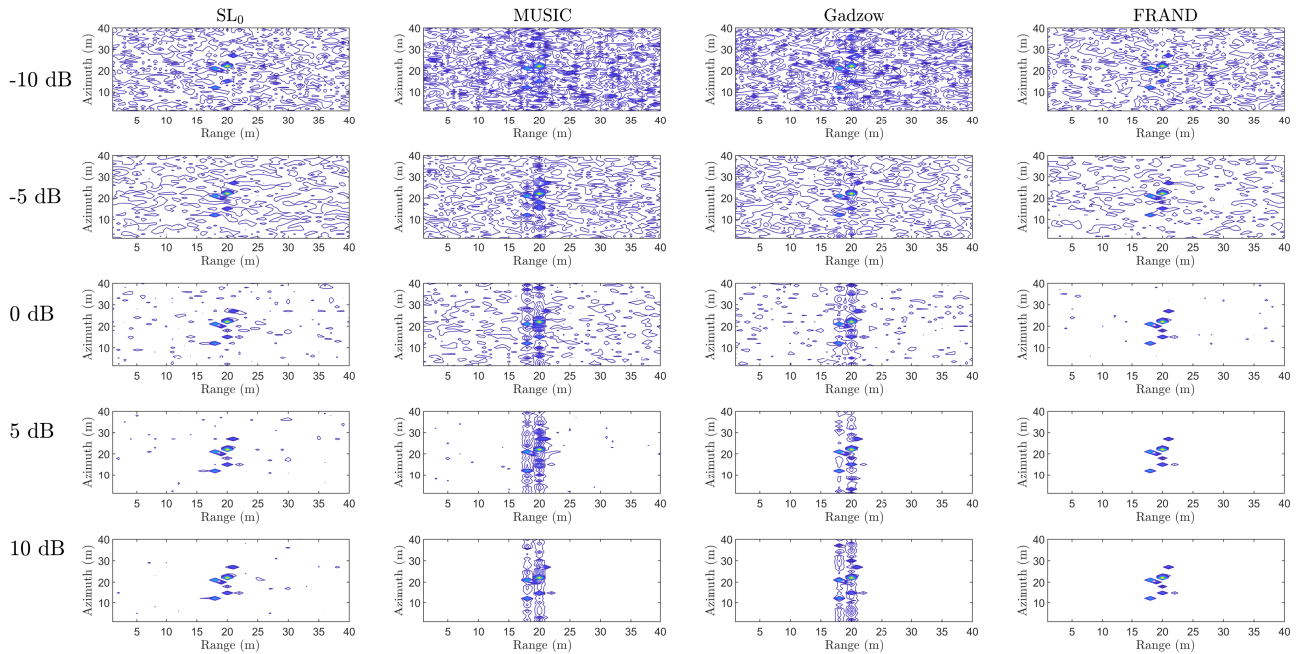


Fig 4. Recovered images of the quadcopter using SL_0 , MUSIC, Cadzow, and FRAND for 100 available samples at SNRs= -10, -5, 0, 5, and 10 dB.

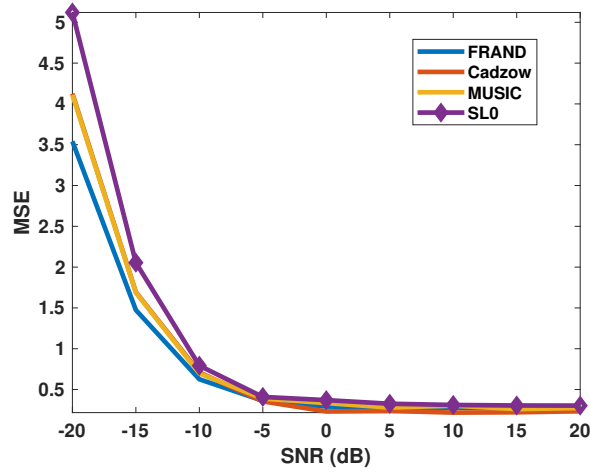


Fig 5. Comparison of FRAND with MUSIC, Cadzow, and SL_0 at SNRs= -10 to 10 dB in terms of MSE.

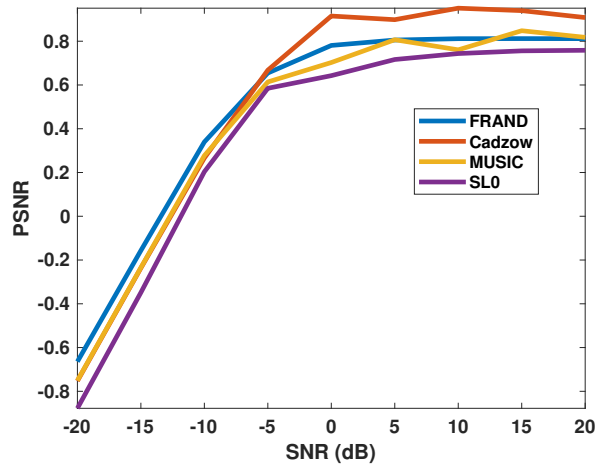


Fig 6. Comparison of FRAND with MUSIC, Cadzow, and SL_0 at SNRs= -10 to 10 dB in terms of PSNR.

superior to the other images at the SNRs lower than -5 dB due to better noise reduction. Moreover, the algorithms are compared in Figure Fig 7 based on the Structural Similarity Index Measure (SSIM), where outperformance of FRAND is observed at different SNRs.

In the next simulation, the execution speeds of different algorithms are compared in Fig 8 for 100 to 500 samples. Although the execution time of FRAND is higher than the others, it can achieve better resolution for ISAR imaging of small targets. It should be pointed out that the execution time of FRAND without implementing the 2D-ADMM algorithm is 7654 seconds for 200 samples, which is reduced to 1.1 seconds by incorporating 2D-ADMM.

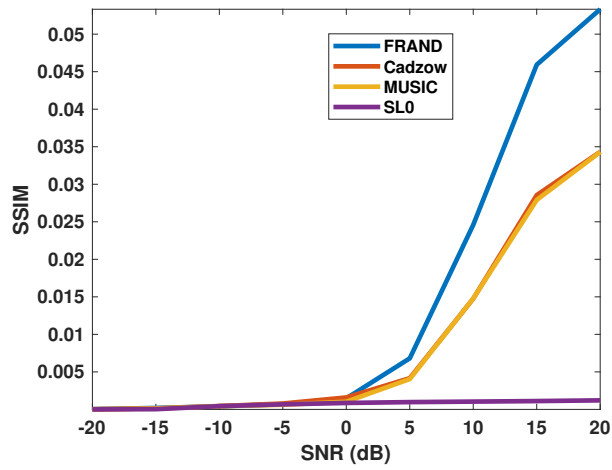


Fig 7. Comparison of FRAND with MUSIC, Cadzow, and SL_0 in term of SSIM criterion and SNRs.

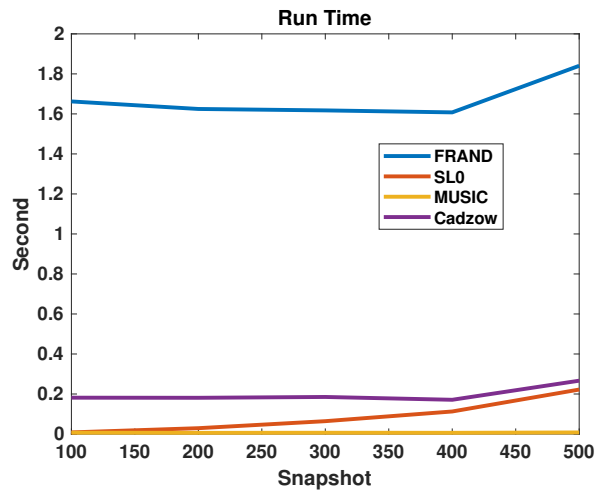


Fig 8. Comparison of running time of FRAND, MUSIC, Cadzow, and SL_0 for available samples from 100 to 500.

5 Conclusion

The FRAND method was proposed based on weighted atomic norm minimization and the 2D-ADMM algorithm to reduce the noise effect and enhance ISAR image resolution in both range and azimuth directions. This super-resolution algorithm was developed based on retrieving more sparse scatterer points of a target in sparse apertures. In this method, the atomic norm of the received signal was written as a linear combination of a set of atoms, which were weighted by a matrix. Then, the 2D-ADMM algorithm was implemented for this problem in order to reduce the number of computations and running time. Simulation results showed the superiority of FRAND over the MUSIC, Cadzow, and SL_0 algorithms at different SNRs in terms of the MSE, PSNR, and SSIM criteria. The results demonstrate the improved efficiency of the proposed method in reducing noise effect and thus increasing the ISAR image resolution.

Author Contributions

Formal analysis: Mohammad Roueinfar.

Methodology: Mohammad Roueinfar., Mohammad Hossein Kahaei.

Supervision: Mohammad Hossein Kahaei.

Validation: Mohammad Hossein Kahaei.

Writing – original draft: Mohammad Roueinfar.

Writing – review and editing: Mohammad Hossein Kahaei.

References

1. Lin M, Meng Z, Luo C, Chen Y. The application of unmanned aerial vehicle oblique photography technology in online tourism design. *PLoS ONE*. 2023 Sep 7;18(9):e0289653. <https://doi.org/10.1371/journal.pone.0289653>.
2. Parra-Ovalle D, Miralles-Guasch C, Marquet O. Pedestrian street behavior mapping using unmanned aerial vehicles. A case study in Santiago de Chile. *PLoS ONE*. 2023 Mar 29;18(3):e0282024. <https://doi.org/10.1371/journal.pone.0282024>.
3. Nemati H, Montazeri A. Analysis and Design of a Multi-Channel Time-Varying Sliding Mode Controller and its Application in Unmanned Aerial Vehicles. *IFAC-PapersOnLine*. 2018; 51(22):244-249. <https://doi.org/10.1016/j.ifacol.2018.11.549>.
4. Sadeghzadeh N. N, Nemati H, Montazeri A. Event-Triggered Based State Estimation for Autonomous Operation of an Aerial Robotic Vehicle. *IFAC-PapersOnLine*. 2019; 52(13):2348-2353. <https://doi.org/10.1109/TSP.2015.2493987>.
5. Lee k, Song K, Sim H, Lee W, Song J, Ryu S, Kang E, Lee H, Lee S. Identification of a Flying Multi-Rotor Platform by High Resolution ISAR through an Experimental Analysis. *International Conference on Radar Systems (Radar 2017)*. 2017; <https://doi.org/10.1109/TIP.2021.3070442>.

6. Lee K, Song K. M, Song J. H, Jung C. H, Lee W. K, Lee M. J, Song Y. K. Implementation of Radar Drone Detection Based on ISAR Technique. *The Journal of Korean Institute of Electromagnetic Engineering and Science*. 2017; 28(2):159-162. <https://doi.org/10.1109/TIP.2021.3070442>.
7. Andrasia P, Radisica T, Mustraa M, Ivosevica J. Night-time Detection of UAVs using Thermal Infrared Camera. *International Conference on Air Transport*. 2017; <https://doi.org/10.1016/j.trpro.2017.12.184>.
8. Coluccia A, Parisi G, Fascista A. Detection and Classification of Multirotor Drones in Radar Sensor Networks: A Review. *Sensors*. 2020; 20(15):4172. <https://doi.org/doi:10.3390/s20154172>.
9. Patel J. S, Fioranelli F, Anderson D. Review of radar classification and RCS characterization techniques for small UAVs or drones. *IET Radar, Sonar and Navigation*. 2018; <https://doi.org/10.1049/iet-rsn.2018.0020>.
10. Ritchie M, Fioranelli F, Griffiths H, Torvik B. Monostatic and bistatic radar measurements of birds and microdrone. *IEEE Radar Conference*. 2016; <https://doi.org/10.1109/RADAR.2016.7485181>.
11. Li Ch. J, Ling H. An investigation on the radar signatures of small consumer drones. *IEEE Antennas and Wireless Propagation Letters*. 2016; 16. <https://doi.org/10.1109/LAWP.2016.2594766>.
12. Zhang Q, Jin Y. Q. Aspects of Radar Imaging Using Frequency-Stepped Chirp Signals. *EURASIP Journal on Applied Signal Processing*. 2006; 85823:1-8. <https://doi.org/10.1155/ASP/2006/85823>.
13. Hu X, Ma Ch, Hu R, Soon Yeo T. Imaging for Small UAV-Borne FMCW SAR. *Sensors*. 2018; 19(87). <https://doi.org/10.3390/s19010087>.
14. Zheng J, Yang T, Liu H, Su T, Wan L. Accurate Detection and Localization of Unmanned Aerial Vehicle Swarms-Enabled Mobile Edge Computing System. *IEEE Transaction on Industrial Informatics*. 2021; 17(7). <https://doi.org/10.1109/TII.2020.3015730>.
15. Gadallah M. B, Abd El-Azeem M. H. Robust extended Cubature Kalman multi-Bernoulli filter for joint detection and tracking ISAR images of small UAVs. *International Journal of Remote Sensing*. 2022; 43(11). <https://doi.org/10.1080/01431161.2022.2105173>.
16. Hai Y, Wang H, Wu J, Pu W, Li Zh, Wang A, Wang D, Huang Y, Yang J. High-Resolution Imaging of Maneuvering Targets in Microwave Photonic ISAR with Improved Variable Mode Decomposition Techniques. *IEEE Transactions on Radar Systems*. 2024; <https://doi.org/10.1109/TRS.2024.3353968>.
17. Ozdemir C. *Inverse Synthetic Aperture Radar Imaging with MATLAB Algorithms*. Hoboken, NJ, USA: Wiley. 2012; <https://doi.org/10.1002/9781118178072>.
18. Roueinfar M, Kahaei M.H. Two-dimensional gridless super-resolution method for ISAR imaging. *Journal of Applied Remote Sensing*. 2023; 17(3) :034502. <https://doi.org/10.1117/1.JRS.17.034502>.
19. Yang L, Zhou J, Xiao H. Super-resolution radar imaging using fast continuous compressed sensing. *Electronic Letter*. 2015; 51(24). <https://doi.org/10.1049/el.2015.2525>.

20. Chandrasekaran V, Zhou J, Xiao H. Super-resolution radar imaging using fast continuous compressed sensing. *Foundations of Computational Mathematics*. 2012; 12:805–849. <https://doi.org/10.1007/s10208-012-9135-7>.
21. Mingjiu L, Lei M, Jianchao M, Wenfeng Ch, Jun Y, Xiaoyan M, Qi Ch. Fast super-resolution sparse inverse synthetic aperture radar imaging via continuous compressive sensing. *IET Signal Processing*. 2021; 16:310–326. <https://doi.org/10.1049/sil2.12092>.
22. Bhaskar B. N, Tang G, Recht B. Atomic Norm Denoising With Applications to Line Spectral Estimation. *IEEE Transaction on Signal Processing*. 2013; 61(23). <https://doi.org/10.1109/Allerton.2011.6120177>.
23. Zhang X, Feng D. An Efficient MUSIC Algorithm Enhanced by Iteratively Estimating Signal Subspace and Its Applications in Spatial Colored Noise. *Remote Sensing*. 2022; 14(17). <https://doi.org/10.3390/rs14174260>.
24. Condat L, Hirabayashi A. Cadzow Denoising Upgraded:A New Projection Method for the Recovery of Dirac Pulses from Noisy Linear Measurements. *Sampling Theory in Signal Processing*. 2015; 14(1):17-41. <https://doi.org/10.1007/BF03549586>.
25. Xu G, Xing M, Yang L, Bao Zh. Joint approach of translational and rotational phase error corrections for high-resolution inverse synthetic aperture radar imaging using minimum-entropy. *IET Radar, Sonar and Navigation*. 2016; 10(3):586-594. <https://doi.org/10.1049/iet-rsn.2015.0356>.
26. Li Y, Chi Y. Off-the-Grid Line Spectrum Denoising and Estimation With Multiple Measurement Vectors. *IEEE Transaction on Signal Processing*. 2015; 64(5):1257-1269. <https://doi.org/10.1109/TSP.2015.2496294>.
27. Feng J, Sun Y, Ji X. High-Resolution ISAR Imaging Based on Improved Sparse Signal Recovery Algorithm. *Wireless Communication and Mobile Computing*. 2021; 5541116. <https://doi.org/10.1155/2021/5541116>.
28. Yang Z, Xi L. Enhancing Sparsity and Resolution via Reweighted Atomic Norm Minimization. *IEEE Transaction on Signal Processing*. 2016; 64(4):995-1006. <https://doi.org/10.1109/TSP.2015.2493987>.